Tip dynamics for equiaxed Al-Cu dendrites in thin samples : phase-field study of thermodynamic effects

Ahmed Kaci Boukellal, Morgane Rouby, Jean-Marc Debierre

Tip dynamics for equiaxed Al-Cu dendrites in thin samples : phase-field study of thermodynamic effects

Ahmed Kaci Boukellal[1,*], Morgane Rouby, Jean-Marc Debierre

Aix-Marseille Université, CNRS, Université de Toulon, IM2NP UMR 7334, 13397 Marseille, France

Abstract

We test the influence of two thermodynamic effects on the dynamics of equiaxed Al-Cu dendrites growth and interactions in thin samples. The first effect results from the nonlinearity of the phase diagram with the copper concentration and the second effect is due to temperature fluctuations. The study relies on three-dimensional phase-field simulations of isothermal solidification in confined samples, for which thickness is of the order of the characteristic diffusion length. We compare the present results with those of a previous study that did not take these thermodynamic effects into account [A. K. Boukellal *et al*, Materialia **1**, (2018)]. We show that including these effects does not affect the scaling laws derived previously. This result strengthens the conclusions already drawn and encourages the application of these scaling laws to predict the behaviour of dendrite tips in more physical situations.

1. Introduction

In order to confer isotropic physical properties to industrial metallic parts like cast engine blocks, equiaxed solidification is preferred in practice. Many materials that are used in such applications belong to the large family of aluminum alloys [1, 2]. We focus here on Al-Cu diluted alloys that have been studied quite intensively over the last decades [3]. One key point concerning the dynamics of growing equiaxed grains is to predict and control

*Corresponding author

[1]Present address: IMDEA Materials Institute, Getafe, Madrid, Spain.

the interactions between two grains that grow toward each-other. Scaling laws that govern the grain growth and the grain-grain interactions in thin samples were recently proposed in reference [4] (hereafter denoted as BEA). Some preliminary results in [5] have shown that a sample of Al−1wt.%Cu, 1000μm in width and length, presents confinement effects for a thickness below 500μm. This thickness is approximately five times the solutal diffusion length $l_s = D/V_m$ where D is the solute diffusion coefficient in the liquid phase and V_m is the maximum tip growth velocity. The samples considered in the present study are 100μm in thickness, thus definitely confined in this direction. The scaling laws are of great relevance because they can be extrapolated to predict the dynamics of equiaxed dendrites in materials containing higher copper concentrations that are not easy to simulate directly. In the present study, phase-field simulations in three dimensions are performed to explore the implications of experimentally relevant thermodynamic effects that were not included originally in BEA, specifically how the growth and interaction scaling laws are affected.

Most of the phase-field simulations of Al-Cu solidification reported in the literature were performed for directional solidification [6–8] or in the case of a constant applied undercooling [9]. Conversely, simulations of solidification in samples cooled homogeneously at a constant rate, as we consider here, are less common [4, 10]. In section 2, we introduce the phase-field model used to simulate isothermal solidification at a constant cooling rate. The constitutive physical equations are discussed together with the corresponding phase-field equations, and their implementation in the numerical code is described. The phase diagram of a diluted alloy is very often assumed linear in numerical studies, while it is usually curved, even for rather low concentrations [11]. It is the first task of the present study to consider the curved Al-Cu phase diagram provided by thermodynamic calculations. The corresponding results are presented and analyzed in section 3. During dendritic growth, the development of secondary branches may have a more or less important influence on the final polycrystalline structure of the material [12, 13], thus on the final properties of the material [2]. In the phase-field simulations, it is necessary to introduce thermodynamic temperature fluctuations by means of a controlled spatio-temporal noise in order to produce realistic dendritic branching. Section 4 is devoted to this second task. The central question of the present study is to quantify the influence of the two thermodynamic effects that are introduced. To do so, the growth and interaction scaling growth laws obtained with and without these two effects are compared in

section 5. Finally, section 6 summarizes our main conclusions.

2. Phase-field model

2.1. Physical equations

We consider aluminum alloys that contain a low copper concentration c_0. For these alloys the partition coefficient $k < 1$, the liquidus slope $m < 0$, so $m(k-1) > 0$.

At a given temperature T_0, the equilibrium concentration at the planar interface taken on the liquid side is given by

$$c_l^0 = (T_0 - T_M)/m, \tag{1}$$

where T_M is the Al melting temperature. In the reference frame where the material is at rest, the copper diffusion equation reads

$$\frac{\partial c}{\partial t} = D\nabla^2 c, \tag{2}$$

where D is the solute diffusion coefficient that will be assumed zero in the solid phase (one-sided model). In addition, two local equations must be verified at any interface point. The first one expresses solute conservation and it imposes the interface normal velocity,

$$V_n = -D\Big(\frac{\partial c}{\partial r}\Big)_\ell, \tag{3}$$

the derivative being taken on the liquid (ℓ) side, in the direction perpendicular to the solid-liquid interface. The second one is the Gibbs-Thomson equation that expresses local thermodynamic equilibrium and that reads in terms of temperatures,

$$T_i = T_M + mc_i - \frac{\Gamma}{\rho} - \frac{V_n}{\mu}. \tag{4}$$

In this equation, ρ is the average radius of curvature, μ the linear kinetic coefficient, and the Gibbs-Thomson constant Γ is related to the chemical capillary length d_0 through

$$d_0 = \frac{\Gamma}{m(k-1)c_l^0}. \tag{5}$$

In the present case, solidification results from a homogeneous cooling at a constant rate $R = 0.5$ K/min. Then the interface temperature $T_i = T_0 - Rt$, where T_0 is set to be the liquidus temperature T_L. Thus, $c_l^0 = c_0$ and the Gibbs-Thomson equation in terms of concentrations reads

$$U_i^* = \frac{c_i - c_0}{(1-k)c_0} = -\frac{d_0}{\rho} - \beta_{\rm kin} V_n + \frac{Rt}{m(k-1)c_0}, \tag{6}$$

where $\beta_{\rm kin} = 1/[m(k-1)c_0\mu]$ is the corresponding kinetic coefficient. In the following, we will use the notation

$$\Theta(t) = -\frac{Rt}{m(k-1)c_0} \tag{7}$$

for the negative undercooling that decreases in time as a result of the sample cooling.

2.2. Phase-field equations

We adopt the quantitative phase-field model introduced by Karma *et al* to simulate the solidification of diluted alloys [14, 15]. Instead of the usual phase-field $-1 \leq \varphi \leq 1$, we use the preconditioned phase-field

$$\psi = \sqrt{2}\tanh^{-1}(\varphi) \tag{8}$$

that was shown to increase numerical precision for a given mesh size [16]. A number of recent phase-field studies confirmed that quantitative results are obtained when using the preconditioned phase-field [4, 17–20].

We follow the usual convention where lengths are scaled by the interface thickness W_0 and times by the relaxation time τ_0. The resulting nondimensional evolution equation for ψ is

$$\begin{aligned}
&[1-(1-k)\Theta]a_s^2\frac{\partial\psi}{\partial t} = a_s^2\Big[\nabla^2\psi - \sqrt{2}\varphi(\vec{\nabla}\psi)^2\Big] \\
&+\sqrt{2}\Big[\varphi - \lambda(1-\varphi^2)(U+\Theta)\Big] + 2a_s\vec{\nabla}a_s\vec{\nabla}\psi \\
&+\frac{\sqrt{2}}{(1-\varphi^2)}\vec{\nabla}\vec{A}.
\end{aligned} \tag{9}$$

As in the case of directional solidification, the imposed undercooling $\Theta(t)$ is also introduced on the left hand side of this equation to prevent the kinetic

coefficient β_{kin} from deviating in time from its imposed value (zero here) [15]. The nondimensional concentration field U is related to the physical concentration field c through

$$U = \frac{f_U(\varphi)c - c_0}{(1-k)c_0}, \tag{10}$$

with

$$f_U(\varphi) = \frac{2}{(1+k) - (1-k)\varphi}. \tag{11}$$

This is the diffuse interface version of the physical definition given in (6): in the liquid phase, $\varphi = -1.0$, so $f_U(\varphi) = 1.0$.

Al-Cu is a material with an atomically rough solid-liquid interface. Thus, the kinetic coefficient β_{kin} should be set to zero for the low solidification velocities considered here. In practice, this is ensured by imposing $\lambda = (75/47)D\tau_0/W_0^2$ for the constant that couples the non-dimensional concentration field U to the phase-field [21]. Since the interface width $W_0 = \xi d_0$ is adjusted by varying the numerical parameter ξ, this fixes the relaxation time to $\tau_0 = (47\sqrt{2}/120)(d_0^2/D)\xi^3$.

In the present work, as in [4, 19, 22, 23], the equation for the time evolution of the phase-field is written in terms of the anisotropy vector $\vec{A}$. This vector appears when, in the original phase-field equation for solidification of a pure melt [21], one rewrites the following sum of three terms as a vector divergence,

$$\sum_{\eta=x,y,z} \partial_\eta \Big[|\vec{\nabla}\varphi|^2 a_s \Big(\frac{\partial a_s}{\partial \varphi_\eta} \Big) \Big] = \vec{\nabla}.\vec{A}. \tag{12}$$

It is worth mentioning that this formulation can be easily implemented for most anisotropy functions of the surface energy, a_s (see Appendix A). For instance, the case of a surface energy anisotropy that leads to facetted growth shapes was recently considered by using this anisotropy vector formulation [23].

Crystalline anisotropy governs the expression of the anisotropy function a_s. Here, we choose to align the Al-Cu cubic crystal axes [1 0 0], [0 1 0] and [0 0 1] with the x, y, and z axes of the numerical mesh. The corresponding anisotropy function reads then [24]

$$a_s = (1 - 3\epsilon_4) + 4\epsilon_4(n_x^4 + n_y^4 + n_z^4), \tag{13}$$

where n_x, n_y, n_z are the components of the unit vector $\vec{n}$ along the normal to the solid-liquid interface and ϵ_4 is the anisotropy strength of the interface energy. As shown in Appendix A, the three components of the anisotropy vector $\vec{A}$ are then

$$A_{x,y,z} = 16\epsilon_4 \frac{(1-\varphi^2)}{\sqrt{2}} |\vec{\nabla}\psi| a_s \Big[(n_x^4 + n_y^4 + n_z^4) - n_{x,y,z}^2 \Big] n_{x,y,z}. \qquad (14)$$

As we neglect solute diffusion in the solid (one-sided model), we must introduce a corrective solute current

$$\vec{j}_{at} = \frac{W_0}{2\sqrt{2}} c_0 (1-k) G \vec{n}, \qquad (15)$$

where

$$G = \frac{1-\varphi^2}{\sqrt{2}} [1 + (1-k)U] \frac{\partial \psi}{\partial t}, \qquad (16)$$

in order to counterbalance the excess of solute trapping and other spurious corrections due to the finite interface thickness W_0 [14, 15]. The evolution equation for the nondimensional concentration field U is then [14, 15]

$$\begin{aligned} \big[(1+k) - (1-k)\varphi\big] \frac{\partial U}{\partial t} &= (1-\varphi) D^* \ \nabla^2 U \\ &\quad - \frac{(1-\varphi^2)}{\sqrt{2}} D^* \ \vec{\nabla}\psi \ \vec{\nabla} U \\ &\quad - \frac{1}{\sqrt{2}} \ \vec{n} \ \vec{\nabla} G + G\Big(1 - \frac{\vec{\nabla}\vec{n}}{\sqrt{2}}\Big), \end{aligned} \qquad (17)$$

where

$$D^* = \frac{D\tau_0}{W_0^2}. \qquad (18)$$

2.3. Implementation

We very closely follow the implementation described in BEA. The main physical parameters of the Al-Cu alloys are gathered in Table 1. It was shown in BEA that the choice $W_0 = 24.0 d_0$ for the interface width gives well converged results, so we also use this value here.

The first step of the work consists in bringing an initial germ to equilibrium for the imposed parameters. To do so, we start from a sphere of radius R_0. We set the phase-field $\psi(\vec{r}, t=0) = -|\vec{r} - \vec{R_0}|/W_0$, the supersaturation

Table 1: Physical parameters of the Al-Cu alloys considered in the simulations.

Symbol	Physical parameter	Value	Unit
D	copper diffusion coefficient in the liquid	3000.0	μm^2/s
T_M	aluminum melting temperature	933.0	K
c_p	aluminium specific heat at melting temperature	2.8×10^{-12}	J/K/μm^3
c_0	copper concentration	$1.0, 1.5, 2.0$	wt.%Cu
ϵ_4	crystal cubic anisotropy	0.01	–
Γ	Gibbs-Thomson coefficient	0.236	Kμm

$U(\vec{r}, t = 0) = -d_0/R_0$ and $\Theta(t = 0) = d_0/R_0$. Then ψ and U are calculated while varying up and down Θ until the V_x along the x axis cancels out. The final state of this step is used as the initial condition in what follows. Mirror (no-flux) conditions are constantly imposed at all the domain boundaries. Thus, it is sufficient to simulate a quarter of the whole sample plane xz, let us say $x \geq 0$ and $z \geq 0$. For the same reason, only one half of the sample thickness is necessary, let us say $y > 0$. Altogether, we only simulate an eighth of the sample and complete it by applying symmetries: the origin of the numerical domain is thus the center of the solid. Due to the no-flux boundary conditions, mirror dendrites develop and progress toward the reference dendrite from the right and from above, causing dendrite-dendrite collisions after some time. As the interface width W_0 is inversely proportional to the copper concentration, the physical mesh size δs varies the same way. We take here $\delta s = hW_0$ with the numerical grid spacing $h = 1.0$. As shown in [16], this choice gives very accurate results for a pre-conditioned phase-field. The dimensions $L \times L \times H$ of the simulated physical domains are the same as in BEA, i. e., $L = 800$, 1000, 1200 μm and $H = 100$ μm. These dimensions are chosen to reproduce the geometry of recent experiments in thin samples, that we want to compare with our simulations [4, 25]. We use the simple Euler time integration scheme and a simple finite difference scheme for the spatial derivates. Then the time step must satisfy the stability condition

$$\delta t \leq \frac{75}{282} \frac{h^2}{\lambda} \tau_0 \tag{19}$$

in three dimensions. The finite difference scheme is accelerated more than 30 times by coding it on a Graphics Processing Unit (GPU). A general purpose GPU is used that is optimized for 32-bit numbers, so all the real numbers we use are implemented as simple precision floats. As discussed in Appendix B, this is not without consequences when a small thermodynamic noise is to be introduced in the code.

3. Thermodynamic phase diagram

3.1. Concentration dependence

In BEA, average estimates of the partition coefficient, $k = 0.14$, and of the liquidus slope, $m = -2.6$K/wt.%Cu, were used. Both estimates were taken from an early representation of the whole Al-Cu phase diagram where the liquidus and the solidus are assumed globally linear for $c_0 < 16$wt.%Cu [26]. However, the phase diagram of Al-Cu alloys is actually not linear, even for concentrations of a few wt.%Cu. The reason is that the assumption of a diluted alloy rapidly loses its statistical justification: for a concentration of $c_0 = 2.0$ wt.%Cu, the probability that two Cu atoms in a randomly diluted alloy are in contact is already about 10 percent. According to recent thermodynamic data [27], the liquidus and solidus are definitely curved, as can be seen in Fig. 1. In order to assess the robustness of the BEA results, the magnitude of the corrections induced by these deviations from linearity has to be carefully estimated.

The first step is to estimate k and m as functions of the copper concentration c. To do so, the available thermodynamic data [27] for the liquidus temperature T_L and for the solidus temperature T_S are plotted in Fig. 1 as functions of c. Both curves are fitted to third-order polynomials,

$$T_L(c) = a_L c^3 + b_L c^2 + c_L c + T_M, \tag{20}$$

and

$$T_S(c) = a_S c^3 + b_S c^2 + c_S c + T_M, \tag{21}$$

The values of (a_L, b_L, c_L) and (a_S, b_S, c_S) are listed in Table 2.

For the alloy nominal concentration $c = c_0$, (20) is used to obtain the corresponding liquidus temperature $T_0 = T_L(c_0)$. Then (21) is used to find c_0' such that $T_S(c_0') = T_0$ (see Fig. 1), and the partition coefficient is given by

$$k = c_0'/c_0. \tag{22}$$

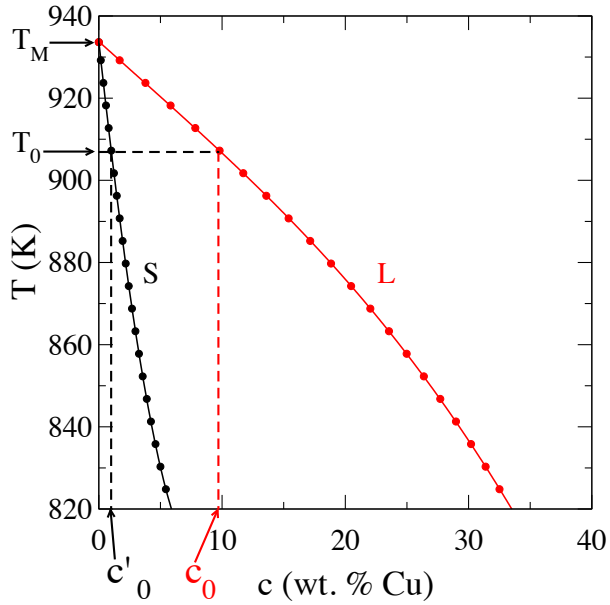

Figure 1: A part of the Al-Cu phase diagram. Markers represent available data from a thermodynamic data base [27]. Continuous lines are fits to third order polynomials giving approximate equations for the liquidus (L) and the solidus (S) lines.

Table 2: The interpolation coefficients (a_L, b_L, c_L) and (a_S, b_S, c_S) to be used with equations (20) and (21) when c expressed in wt.%Cu divided by 100.

a_L	b_L	c_L	a_S	b_S	c_S
-826.3	69.952	-270.34	35974.0	11929.0	-2758.3

For the same concentration c_0, the liquidus slope is given by $\left[\partial T_L/\partial c\right]_{c=c_0}$, that is

$$m = 3a_L c_0^2 + 2b_L c_0 + c_L. \tag{23}$$

The resulting values of k and m are listed in Table 3 for a few copper concentrations c_0. In the range of concentrations considered in the present study ($c_0 \leq 2$ wt.%Cu), the partition coefficient is roughly constant, $k = 0.098$, and the liquidus slope decreases slightly but remains close to $m = -2.7$ K/wt.%Cu. Both values definitely differ from the estimates used in BEA. Regarding the imposed undercooling defined in (7), one sees that, at given time t and concentration c_0, $\Theta(t)$ is roughly 8 percent smaller in the present case than in BEA, so dendritic growth is expected to be slower.

Table 3: Partition coefficient k and liquidus slope m for Al-Cu alloys at different copper concentrations c_0 up to the eutectic concentration (last entry).

c_0 (wt.%Cu)	k	m (K/wt.%Cu)
0.5	0.098	−2.697
1.0	0.098	−2.692
1.5	0.098	−2.688
2.0	0.098	−2.685
4.0	0.099	−2.687
10.0	0.103	−2.811
20.0	0.118	−3.415
33.1	0.172	−4.956

3.2. Results

Figure 2 shows six snapshots illustrating the time evolution of a dendrite obtained in a $1000 \times 1000 \times 100$ μm^3 sample for a concentration $c_0 = 1.0$ wt.%Cu. As in BEA, the production of secondary arms is very limited because thermal fluctuations are not included. One recovers the three main growth regimes already observed in BEA:

1. slow growth (0-60 s): the undercooling is proportional to time and cooling rate R, and so it is very low at the beginning of the growth.
2. fast growth (60-90 s): the nearly spherical seed turns into a cross-shaped dendrite with two primary arms along x and z axes. The two primary arms grow fast and almost freely because the undercooling is high and the available space is large enough.
3. poisoned growth (90-150 s): the two primary arms reach the domain boundaries. They stop growing and they broaden. Secondary arms develop and fill the space.

Figure 3 represents the dendrite tip velocity V_x measured along the horizontal direction x as a function of time. In comparison with the curve that was obtained in BEA, the maximum velocity is lower and it arises at later time in the present study because the instantaneous undercooling is smaller. Besides these quantitative differences, the two curves are very similar.

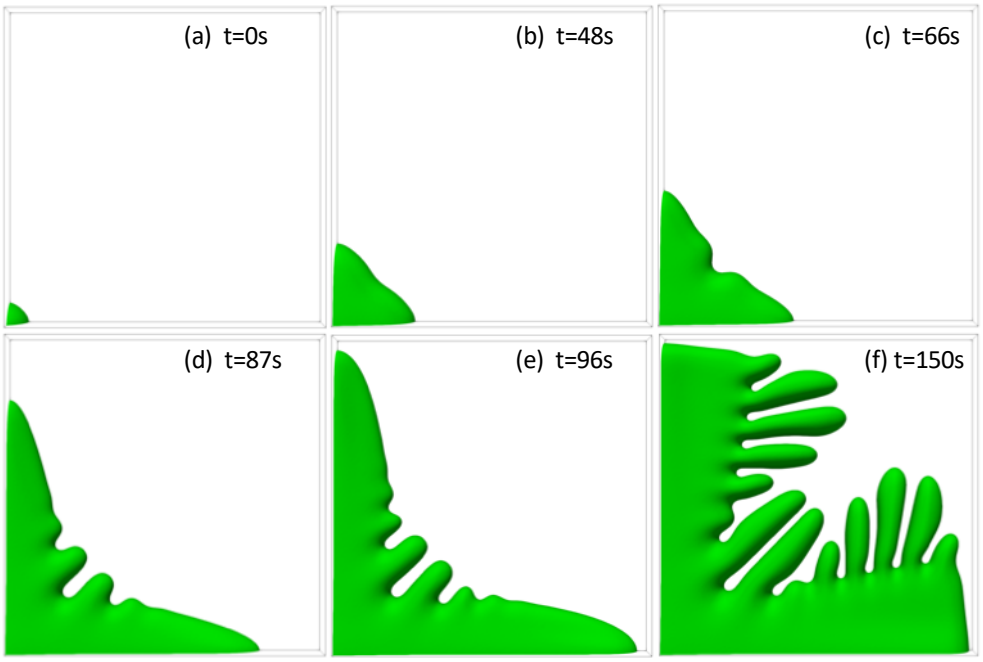

Figure 2: Time evolution of a dendrite obtained in a $1000 \times 1000 \times 100$ μm^3 sample for a concentration $c_0 = 1.0$ wt.%Cu (see the second line in Table 3 for the phase diagram parameters k and m).

4. Thermal fluctuations

4.1. Spatiotemporal noise

Our second point of interest is the role of thermal fluctuations the mean square of which is given by

$$\left\langle (\Delta T)^2 \right\rangle = \frac{k_B T_0^2}{c_p \Delta \mathcal{V}}, \tag{24}$$

with k_B the Boltzmann constant, c_p the Al specific heat (table 1), and $\Delta\mathcal{V}$, the fluctuation volume [28]. At the scale of one mesh element, $\Delta\mathcal{V} = (\delta s)^3 \simeq 16.2$ μm^3, one expects thermodynamical temperature fluctuations to be of the order of 5×10^{-4} K for the alloy considered here.

So far, we neglected the thermal fluctuations, so secondary branches did not appear near the dendrite tip during the fast growth regime. Including physically reasonable thermal fluctuations should provoke branching. Moreover, since branching is not deterministic, an asymmetry between the two

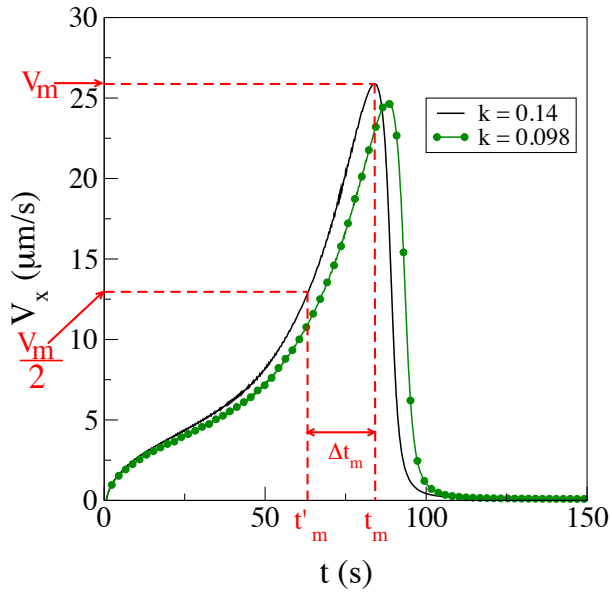

Figure 3: Velocity V_x of the dendrite tip as a function of time (curve with markers). A unique concentration, $c_0 = 1.0$ wt.%Cu, and a unique sample size $L = 1000$ μm is considered. The curve corresponding to BEA ($k = 0.14$) is shown for comparison (without markers).

growth directions x and z may arise. The question we want to decide is wether this asymmetry would ultimately lead to different growth laws in the two directions and/or in different simulations.

In our code, the fluctuations of the sample temperature $T(t) = T_0 - Rt$ are imposed by the means of a numerical spatiotemporal noise,

$$T(\vec{r}, t) = (T_0 - Rt)\{1 + F_0[2\eta(\vec{r}, t) - 1)]\}, \tag{25}$$

where F_0 is the noise amplitude and $\eta(\vec{r}, t)$ is a pseudo-random number that is picked for each mesh point $\vec{r}$ and each time t from a uniform distribution over the range $[0, 1)$. As a consequence, the dimensionless undercooling introduced in equation (7) now becomes

$$\Theta(\vec{r}, t) = \frac{-Rt + A_0(T_0 - Rt)}{(k-1)mc_0}, \tag{26}$$

where $A_0 = F_0[2\eta(\vec{r}, t) - 1)]$ is a random number between $-F_0$ and $+F_0$. In the following, we impose a noise amplitude $F_0 = 1.0 \times 10^{-4}$. Noting

that Rt remains negligible as compared to T_0 here, this leads to temperature fluctuations of the order of $F_0 T_0 \simeq 0.1$ K per time step. Taking the time correlations into account [29, 30], we obtain independent fluctuations of typical amplitude $F_0 T_0 \sqrt{\delta t/\tau_0} \simeq 0.0035$ K which is about 7 times higher than the thermodynamic value calculated from equation (24). This enhancement of the thermal fluctuations is deliberately made here because we want to decide wether significant effects will result or not. As shown in Appendix B, studying the case of physical thermal fluctuations would in addition require to use the double precision representation of real numbers. The code would thus become much slower, unless 64-bit GPUs are used. Let us stress that the present noise differs in nature from the one that is usually imposed in phase-field simulations. While the latter is imposed on the phase and/or the concentration fields that are computed from the time evolution equations [29, 30], the former concerns the fluctuations of a control parameter (the imposed temperature).

Figure 4 shows six snapshots illustrating the evolution of a dendrite obtained with the thermal noise just discussed and for the k and m values used in BEA (linear phase diagram). Here again, the three main growth regimes are obtained. It is worth noting that during regime 2, in which primary arms grow freely, secondary arms do appear now because of the thermal fluctuations (see panel d). During this regime, secondary arms did not appear in our previous simulations without noise.

4.2. Growth velocity

Figure 5 shows the velocities of two dendrite tips when thermal noise is included and when it is not. This figure also shows the velocity differences $\Delta V_{x,z}$ between the two curves. Both velocity curves (with and without noise) show the same global behaviour: a steady increase of the velocity until it reaches a maximum, then a sharp decrease followed by a slow convergence to zero. Obviously, the spatiotemporal noise affects more the tip velocity near its maximum. In the specific case shown in figure 5, the tip that progresses along the x axis is accelerated while the tip along the z axis is decelerated as compared to the case without noise. We obtained nine comparable figures by performing a single simulation for each choice of (L, c_0). It would have been interesting to average $\Delta V_{x,z}$ for each (L, c_0) over a number of simulations with different realizations of the spatiotemporal noise but this represented a very time-consuming task that was beyond the scope of the present study. For the different choices of (L, c_0), one sometimes observes the same effect

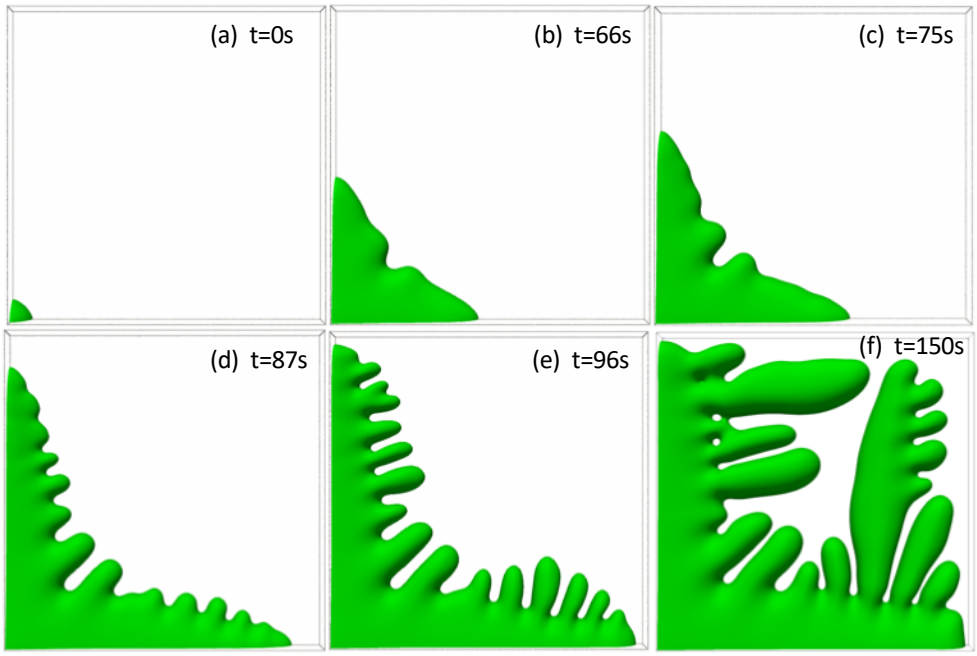

Figure 4: Time evolution of a dendrite obtained in a $1000 \times 1000 \times 100$ μm^3 sample for $c_0 = 1.0$ wt.%Cu, $k = 0.14$ and $m = -2.6$ K/wt.%Cu. Noise amplitude $F_0 = 1.0 \times 10^{-4}$.

as in figure 5 and sometimes the opposite one, so the average of the velocity differences $\Delta V_{x,z}$ on the different (L, c_0) simulations is close to zero (see figure 6). It is interesting to note that, even for the large noise amplitude considered here, there is no dramatic change of the tip dynamics but rather fluctuations around the mean behavior obtained without noise.

5. Growth scaling laws

In BEA, we characterized the time evolution of the dendritic tip velocity V through the maximum velocity reached, $V = V_m$, and through the time Δt_m necessary for V to increase from $V_m/2$ to V_m (see figure 3). We obtained scaling laws giving both quantities as functions of the scaling parameters L^a/c_0^α and L^b/c_0^β, respectively. The scaling exponents (a, α) were obtained by fitting the numerical values of V_m. On the other hand, (b, β) were deduced from the result $\Lambda = L_m/L =$cst, where $L_m = V_m \Delta t_m$ and L is the box length. In the present work, we plot the values of V_m and Δt_m as functions of the same scaling parameters as in BEA, both for a linear phase diagram in the

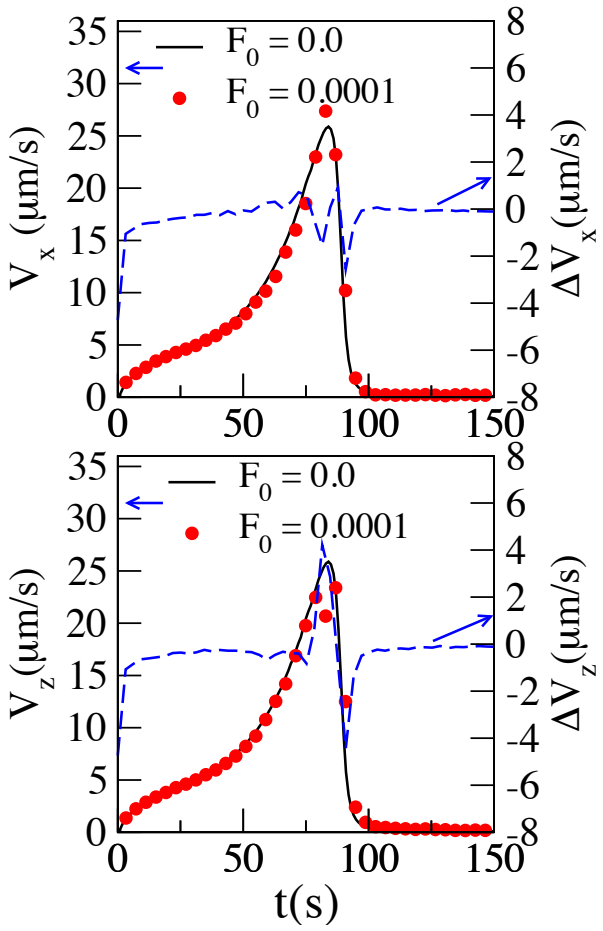

Figure 5: Time evolution of the tip velocities (red disks) along x and z for the dendritic growth with thermal noise illustrated in Fig. 4. The represented data are obtained for the parameter choice $(L, c_0) = (1000\ \mu\text{m}, 1.0\ \text{wt.\%Cu})$. For comparison, the results obtained without noise are represented by continuous curves (black lines). The irregular sawtooth curves represent the differences between the velocities obtained with and without noise (dashed blue lines).

case of imposed thermal fluctuations and for a realistic curved phase diagram.

Figure 7 shows the variations of V_m and Δt_m with the same scaling parameters as in BEA. As could be expected, the scaling laws derived previously fit the present data as well, with slight deviations due to numerical reasons. On one hand, in the case of a linear phase-diagram, one can notice that the results in presence of a thermal noise are in good agreement with those in

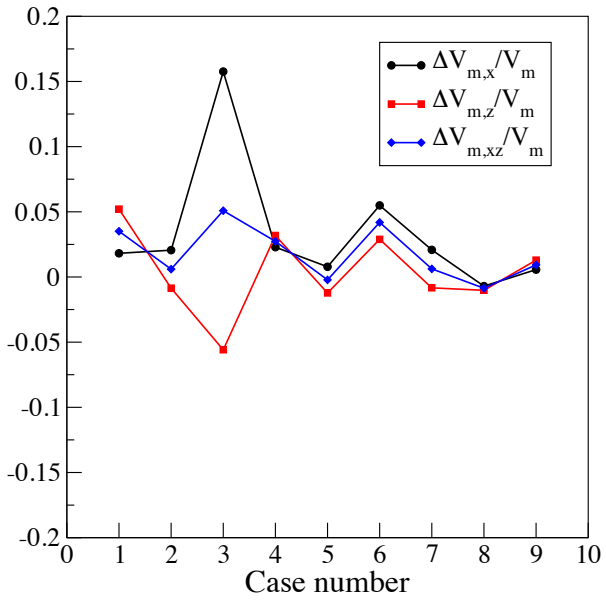

Figure 6: Velocity difference $\Delta V_x/V_m = (V_{m,x} - V_m)/V_m$, where V_m represents the maximum growth velocity without noise and $V_{m,x}$ represents the maximum growth velocity along the x axis, for an imposed thermal noise of amplitude $F_0 = 1.0 \times 10^{-4}$. The different cases correspond to the nine couples (L, c_0) considered in this work. ΔV_z is the corresponding velocity difference along the z axis and ΔV_{xz} the average over the x and z axes.

BEA. Indeed, taking into account the thermal noise in the present work does not affect the growth regimes described in section (4.2). One can see that although the amplitude of the fluctuations imposed in the code is 7 times higher than the thermodynamic one predicted by Equation (24), the noise induces only slight deviations of V_m and Δt_m. On the other hand, we also notice a good agreement with the results in BEA when a thermodynamic phase diagram is considered. Let us remark that for the dilute Al-Cu alloys considered here, the product $m(k-1)$ is only increased by a factor of 1.088 for a given c_0 in the present case as compared to BEA. This small variation is thus expected to weakly affect the dynamics of the system as W_0 and $\Theta(t)$ keep almost the same values in both cases. Considering the three series of the data altogether, one finds that $\Lambda \approx 0.537$ instead of $\Lambda \approx 0.546$ quoted in BEA (that was readjusted after a more systematic data analysis to $\Lambda \approx 0.550$). This result strengthens the conclusions drawn previously stating that $V_m \Delta t_m$ is only a function of the distance $2L$ between the grains whose

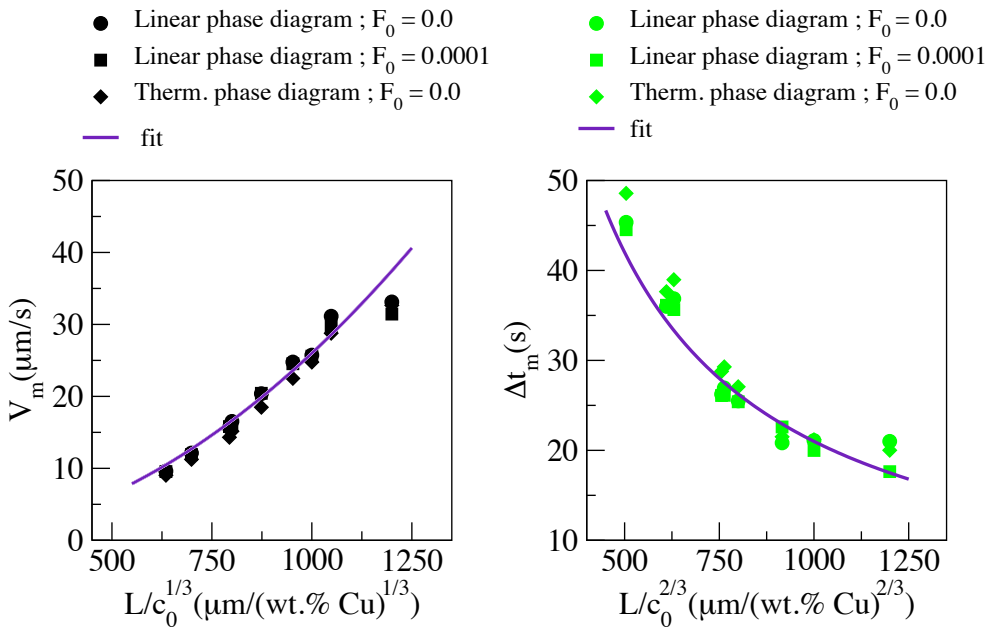

Figure 7: Scaling of the data obtained for different phase diagrams and different noise amplitudes F_0. The solid curves are fits of the data for the linear phase diagram without noise (from BEA). These fits give the following rounded values for the scaling exponents: $a = 2$, $\alpha = 2/3$, $b = -1$, and $\beta = -2/3$.

primary arms grow toward each other. Altogether, the results obtained in this section confirm that extrapolation of our scaling laws to the concentrations of industrial or experimental interest remains possible even in presence of thermal fluctuations and in the case of a thermodynamic phase diagram. As a general remark from a numerical point of view, the results obtained in the case of a thermodynamic phase diagram can be reproduced by the code developed in BEA provided that the product $m(k-1)c_0$ and W_0 are adjusted so as to be identical in both cases. However, the results will correspond to different physical systems as c_0 will be shifted on the phase diagram.

6. Summary and conclusion

We have presented the numerical results of 3D phase-field simulations of Al-Cu equiaxed growth. Two thermodynamic effects have been considered and their implications on the scaling behaviour of the dendrite tip growth dynamics has been explored.

First, a curved thermodynamic phase diagram has been considered, instead of the linear diagram approximation that is usually taken. The partition coefficient k and the product $m(k-1)$ are lower in the former case (m is the liquidus slope). As a result, growth is slower than in the linear approximation. This shows that taking into account a thermodynamic phase diagram in the phase-field model is required to make a very quantitative comparison with experiment.

Second, keeping the linear phase diagram, spatiotemporal noise has been imposed to describe the thermal fluctuations that renders growth less deterministic. Developed secondary branches are indeed obtained and the curves giving the growth velocity as a function of time differ from one dendrite tip to the other. This partly explains the unique character of the dendrite evolutions observed in experiments [4, 25].

Finally, the scaling laws derived in BEA, giving the maximum dendritic growth rate V_m and the characteristic growth time Δt_m as functions of the copper concentration c_0 and the available space L have been independently tested for both thermodynamic effects. Although consideration of a thermodynamic phase diagram is important at higher concentrations and the presence of thermal fluctuations is essential at lower concentrations, the scaling laws remain valid even in the presence of these thermodynamic effects. A natural extension of this work would be to combine both thermodynamic effects and check the accuracy of the scaling laws in these conditions that are closer to the experimental ones.

Appendix A. Anisotropy vector for the surface free energy

In this appendix, we give the general expression of the anisotropy vector $\vec{A}$ as a function of the preconditioned phase-field ψ. We obtain explicit expressions of three components A_x, A_y, and A_z for the case of a cubic anisotropy. Using the preconditioned phase-field

$$\psi = \sqrt{2}\tanh^{-1}(\varphi) \tag{A.1}$$

and its first derivatives

$$\partial_\eta \varphi = \frac{1}{\sqrt{2}}(1-\varphi^2)\partial_\eta \psi, \tag{A.2}$$

where $\eta = x, y, z$, one obtains

$$A_\eta = \frac{1-\varphi^2}{\sqrt{2}}|\vec{\nabla}\psi|^2 a_s \frac{\partial a_s}{\partial \psi_\eta}. \tag{A.3}$$

Introducing the components

$$n_\eta = -\frac{\partial_\eta \psi}{|\vec{\nabla}\psi|} \tag{A.4}$$

of the unit vector $\vec{n}$ normal to the solid-liquid interface, the last term in eq. A.3 becomes

$$\frac{\partial a_s}{\partial \psi_\eta} = \sum_{\zeta=x,y,z} \frac{\partial n_\zeta}{\partial \psi_\eta} \cdot \frac{\partial a_s}{\partial n_\zeta} = \frac{1}{|\vec{\nabla}\psi|} \sum_{\zeta=x,y,z} (n_\eta n_\zeta - \delta_{\eta,\zeta}) \frac{\partial a_s}{\partial n_\zeta}. \tag{A.5}$$

with $\delta_{\eta,\zeta} = 1$ if $\eta = \zeta$, and 0 otherwise. Thus,

$$A_\eta = \frac{(1-\varphi^2)}{\sqrt{2}} |\vec{\nabla}\psi| a_s \sum_{\zeta=x,y,z} (n_\eta n_\zeta - \delta_{\eta,\zeta}) \frac{\partial a_s}{\partial n_\zeta}. \tag{A.6}$$

The anisotropy vector can thus be derived for any continuous function $a_s(n_x, n_y, n_z)$ representing the anisotropy function. In the present work, we study the growth of Al-Cu alloys, that adopt a cubic symmetry in the solid phase. In this case, the anisotropy function simply reads

$$a_s(\vec{n}) = (1 - 3\epsilon_4) + 4\epsilon_4 (n_x^4 + n_y^4 + n_z^4), \tag{A.7}$$

and its partial derivatives are

$$\frac{\partial a_s}{\partial n_\zeta} = 16\epsilon_4 n_\zeta^3. \tag{A.8}$$

Then the three components of the anisotropy vector are

$$A_\eta = 16\epsilon_4 \frac{(1-\varphi^2)}{\sqrt{2}} |\vec{\nabla}\psi| a_s \; n_\eta \Big[(n_x^4 + n_y^4 + n_z^4) - n_\eta^2 \Big], \tag{A.9}$$

with $\eta = x, y, z$.

Appendix B. Significative range of fluctuations for a uniform spatiotemporal noise of amplitude F_0

In this appendix, we obtain bounds for the range of random fluctuations that it is possible to represent on a computer and we give advices to implement fluctuations on GPUs. In equation (25), the thermal fluctuations of the imposed temperature T are introduced by multiplying T by a factor

$$1 + aF_0, \tag{B.1}$$

where F_0 is the fluctuation amplitude and a is a pseudo-random number picked from a uniform distribution over the range $[-1, 1)$. For the sake of the argument, let us assume that one exactly has

$$F_0 = 10^{-m}, \tag{B.2}$$

with m a positive integer. If s represents the number of significative digits of the floating-point representation used for real numbers,

$$S = 10^{-s} \tag{B.3}$$

is the smallest number that can be added to or subtracted from 1 without totally falling in rounding errors. Thus, the imposed fluctuations will be masked by rounding errors if

$$|aF_0| < S, \tag{B.4}$$

that is

$$|a| < \frac{S}{F_0}, \tag{B.5}$$

or finally

$$|a| < 10^{m-s}. \tag{B.6}$$

This means that the corresponding range of small fluctuations is always out of reach in numerical simulations.

Our numerical simulations have been performed on a GPU that is very fast for simple precision ($s = 6$) but much slower for double precision ($s = 15$). For this reason, we used simple precision floats. Thus, for the noise amplitude we used ($m = 4$), the fluctuation range $-0.01 < a < 0.01$ is not described correctly. Physical fluctuations are roughly 10 times lower ($m = 5$). In this case, 10 percent of the fluctuation interval would not be described correctly, which is not acceptable. The solution would be to switch to double precision but, as just said, the computing time would be increased significantly. It is thus advisable, when one needs to simulate physical thermal fluctuations, to use GPUs that are optimized for double precision.

Acknowledgments We wish to express our gratitude to Guillaume Reinhart for directing us to the Thermo-Calc data base, and to Damien Touret for his

critical reading of the manuscript. The project leading to this publication has received funding from Excellence Initiative of Aix-Marseille University A*MIDEX, a French Investissements d′Avenir programme. We thank the French Centre for Spatial Research (CNES) for constant financial support.

References

[1] S. S. Miller, L. Zhuang, J. Bottema, A. J. Wittebrood, P. De Smet, A. Haszlar, and A. Viregge, Mater. Sci. Eng. A **280**, 37 (2000).

[2] J. G. Kaufman and E. L. Rooy, *Aluminum Alloy Castings: Properties, Processes and Applications* (AMS International, Materials Park, Ohio, 2004)

[3] L. F. Mondolfo, *Aluminum Alloys: Structure and Properties* (Butterwoths, London, 1976), pp. 693-758

[4] A. K. Boukellal, J.-M. Debierre, G. Reinhart, and H. Nguyen Thi, Materialia **1**, 62 (2018).

[5] A. K. Boukellal, *Isothermal solidification of Si and Al-Cu : 3D phase-field simulations*, Ph.D thesis, Aix-Marseille University (2019)

[6] A. Badillo and C. Beckermann, Acta Mat. **54**, 2015 (2006).

[7] G. Boussinot and M. Apel, Acta Mat. **122**, 310 (2017).

[8] A. J. Clarke, D. Tourret, S. D. Imhoff, P. J. Gibbs, K. Fezzaa, and A. Karma, Acta Mat. **129**, 203 (2017).

[9] F. Li, W. Zhi-Ping, Z. Chang-Sheng, and L. Yang, Chin. Phys. B **18**, 1985 (2009).

[10] Y. Chen, D. Z. Li, B. Billia, H. Nguyen-Thi, X. B. Qi, and N. M. Xiao, ISIJ Int. **54**, 445 (2014).

[11] H. Okamoto, *Phase Diagrams for Binary Alloys, 2nd Edition* (ASM International, Materials Park, Ohio, 2010)

[12] B. Bőttger, J. Eiken, and M. Apel, J. Comput. Phys. **228**, 6784 (2009).

[13] K. P. Young and D. H. Kirkwood, Metall. Trans. A **6**, 197 (1975).

[14] A. Karma, Phys. Rev. Lett. **87**, 115701 (2001).

[15] B. Echebarria, R. Folch, A. Karma, and M. Plapp, Phys. Rev. E **70**, 061604 (2004).

[16] K. Glasner, J. Comput. Phys. **174**, 695 (2001).

[17] J.-M. Debierre, R. Guérin, and K. Kassner, Phys. Rev. E **88**, 042407 (2013).

[18] N. Bergeon, D. Tourret, L. Chen, J.-M. Debierre, R. Guérin, R. Ramirez, B. Billia, A. Karma, and R. Trivedi, Phys. Rev. Lett. **110**, 226102 (2013).

[19] J. Ghmadh, J.-M. Debierre, J. Deschamps, M. Georgelin, R. Guérin, and A. Pocheau, Acta Mat. **74**, 255 (2014).

[20] T. Z. Gong, Y. Chen, Y. F. Cao, X. H. Kang, D. Z. Li, Comput. Mater. Sci. **147**, 338 (2018).

[21] A. Karma and W. J. Rappel, Phys. Rev. E **57**, 4323 (1998).

[22] J. Ghmadh, J.-M. Debierre, M. Georgelin, R. Guérin, and A. Pocheau, Phys. Rev. E **98**, 052802 (2018).

[23] A. K. Boukellal, A. K. Sidi Elvalli, and J.-M. Debierre, J. Cryst. Growth **522**, 37 (2019).

[24] J. J. Hoyt, M. Asta, and A. Karma, Phys. Rev. Lett. **86**, 5530 (2001).

[25] A. Bogno,H. Nguyen-Thi, G.Reinhart, B. Bilia B, and J. Baruchel, Acta. Mat. **61**, 1303 (2013).

[26] R. Hultgren, P. R. Desai, D. T. Hawkins, M. Gleiser, and K. K. Kelley, *Selected Values of the Thermodynamic Properties of Binary Alloys* (American Society for Metals, Metals Park, Ohio, 1973), pp. 151-153

[27] Thermo-Calc Software TTAL7 Al-Alloys database version 7.1

[28] L. Landau and E. Lifshitz, Statistical Physics *Course of Theoretical Physics*, Vol. 5, p.80 (Pergamon Press, Oxford, 1980).

[29] A. Karma, W. J. Rappel, Phys. Rev. E **60**, 3614 (1999).

[30] B. Echebarria, A. Karma, S. Gurevich S, Phys. Rev. E **81**, 021608 (2010).